

Underwater 3D Reconstruction Using Light Fields

Yuqi Ding¹ Yu Ji² Jingyi Yu³ Jinwei Ye¹

¹Louisiana State University ²DGene U.S.A. ³ShanghaiTech University

Abstract

Underwater 3D reconstruction is challenging due to the refraction of light at the water-air interface (most electronic devices cannot be directly submerged in water). In this paper, we present an underwater 3D reconstruction solution using light field cameras. We first develop a light field camera calibration algorithm that simultaneously estimates the camera parameters and the geometry of the water-air interface. We then design a novel depth estimation algorithm for 3D reconstruction. Specifically, we match correspondences on curved epipolar lines caused by water refraction. We also observe that the view-dependent specular reflection is very weak in the underwater environment, resulting in the angularly sampled rays in light field having uniform intensity. We therefore propose an angular uniformity constraint for depth optimization. We also develop a fast algorithm for locating the angular patches in the presence of non-linear light paths. Extensive synthetic and real experiments demonstrate that our method can perform underwater 3D reconstruction with high accuracy.

1. Introduction

Reconstructing the 3D structure of underwater scenes is of great interest to many fields in marine science and engineering, including underwater archaeology [20, 30, 53], marine biology [13, 16], underwater robotics [23, 36], and seafloor mapping [33, 37] *etc.* As most electronic devices cannot be directly submerged in water and need to be placed inside a watertight housing, a water-air interface is inevitable. The refraction of light that occurs at the water-air interface violates the fundamental assumption of most computer vision algorithms that light propagates along a straight line. The problem of underwater 3D reconstruction is therefore highly challenging.

Many existing solutions use conventional cameras for underwater 3D reconstruction. Classical algorithms, such as multi-view stereo [11, 17, 10] and structure from motion [41, 24, 9, 21], are adapted to the underwater environment by considering the refractive geometry [46, 11, 45]. In this paper, we present a method that uses compact light field

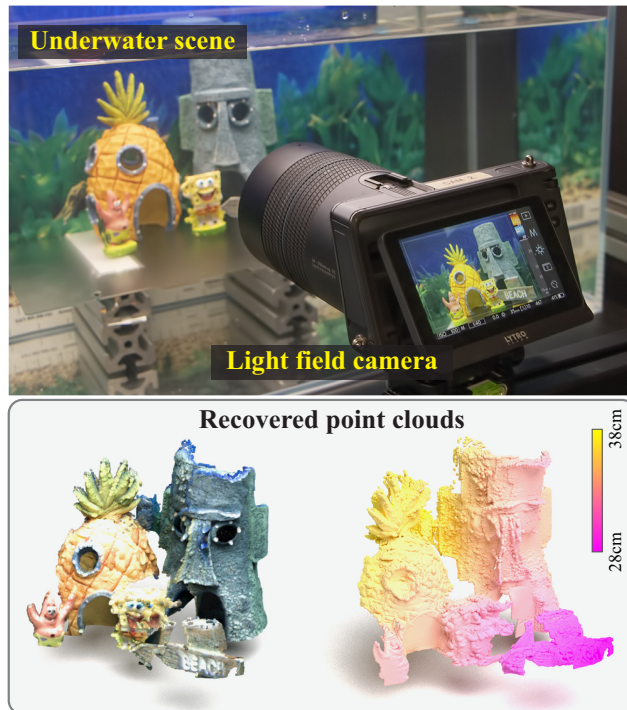


Figure 1. Underwater 3D reconstruction using a light field camera. Top: our experimental setup. Bottom: our reconstructed point cloud of the underwater scene, visualized with the color texture (left) and the color-coded depths (right).

cameras for high-quality underwater 3D reconstruction. By inserting a microlens array in front of the sensor to emulate an array of pinholes, the compact light field camera can be viewed as a multi-view device [35]. As the converging rays are spread out by the microlenses, the light field images also record angular samples from a scene point. Our method exploits the properties of both light field images and underwater scenes for depth estimation. Specifically, we show that the unique “non-specular” reflectance property of underwater scenes [40, 14, 43] imposes useful constraints on the light field angular samples, which greatly improves the performance of underwater depth estimation.

Here we consider the setting that an in-air light field camera (either above the water surface or inside a watertight housing) capturing a scene submerged in water through a

flat water-air interface. We first design an algorithm to calibrate the light field camera in this underwater setting. Our calibration algorithm considers the refraction at the water-air interface. It simultaneously estimates the camera intrinsics, extrinsics, and water-air interface parameters, which includes the geometry of the interface and the refractive index of water. We then develop an optimization framework for underwater depth estimation. Our framework utilizes both the spatial and angular constraints of a light field image. In particular, we account for the color and gradient consistency across the light field sub-aperture images. As the epipolar lines are curved due to refraction [11], we first find the epipolar curves by back-projecting the underwater rays to all sub-aperture images. We then match correspondences along the epipolar curves for depth estimation. In addition, we notice the fact that underwater scenes generally exhibit very weak view-dependent specular reflection (*i.e.*, “non-specular” reflectance) [40, 14, 43]. As result, the light field angular samples should have uniform intensity. We then propose a new angular uniformity constraint that minimizes the variance of an angular patch to improve depth optimization. As the underwater rays are bent, locating the corresponding angular patches is highly computationally expensive. We then develop a fast algorithm based on first-order approximation to improve efficiency.

We perform extensive synthetic and real experiments to demonstrate that our method is highly accurate and reliable. We evaluate both the calibration algorithm and the depth estimation algorithm. We compare with state-of-the-art light field based methods, and show that our approach is more accurate in reconstructing underwater scenes.

2. Related Work

Underwater 3D Reconstruction. Recovering the 3D of underwater scenes is of great interest to the marine research [53, 16, 36, 37]. Many classical computer vision algorithms, including multi-view stereo [11, 17, 10], structure-from-motion (SfM) [41, 24, 9, 21], and structured light scanning [32, 39], are extended to underwater applications. Notably, Chari and Sturm [11] derive the multi-view geometry in refractive medium, and find that the epipolar lines are curved due to refraction. Chadebecq *et al.* [9, 10] consider multiple refractive planes to model relative camera motions, and solve SfM for underwater scenes. Asano *et al.* [2, 3] leverage different absorption rate of near-infrared light for depth sensing in the water. Several methods jointly recover the 3D of the water surface and the underwater scene with defocus cue [54] or multi-view cue [38]. In this paper, we use a light field camera as the acquisition device, and develop algorithms for calibration and 3D reconstruction for underwater applications.

Light Field Imaging. Light field images record 4D spatial and angular samples of a scene. Due to the multi-view nature, light field images are widely used for image synthesis and 3D reconstruction applications, including post-refocusing [34, 29, 48], novel view synthesis [27, 8, 28], and depth reconstruction [44, 50, 22]. To capture a light field, one can either use a camera array [52, 49] that directly captures a grid of images, or a compact light field camera [35, 51] that uses a microlens array in front of the sensor for angular sampling. In this work, we use the microlens-based compact light field camera. Many methods are designed for calibrating a compact light field camera. Dansereau *et al.* [15] derive a 10-parameter intrinsic model to map pixels in a light field image to rays in 3D space. Zhang *et al.* [55] reduce the number of intrinsic parameters with a new ray-space projection model. Bok *et al.* [5, 6] utilize the line features in raw microlens images for more feature extraction. However, all these methods consider the calibration problem in air, which ignores the refraction of light in underwater imaging. Here we develop an underwater calibration method that also estimates parameters of water-air interface, besides the intrinsics and extrinsics. We also leverage the light field angular samples for better underwater 3D reconstruction.

There are some light field based methods developed for underwater applications. Some focus on tackling the low visibility and color distortions of underwater images [42, 47]. Skinner *et al.* [42] develop a fast underwater 3D reconstruction solution using a light field camera. However, this method only accounts for the attenuation of light, but neglects the refraction. It is therefore prone to large errors.

Underwater Camera Calibration. Lavest *et al.* [26] derive compensated lens models when using a camera underwater, and find that the magnifying effect of water refraction is equivalent to scaling the in-air focal length with the fluid’s refractive index. Treibitz *et al.* [46, 45] solve a simplified underwater calibration problem with a frontal-parallel refraction plane and known refractive index. Agrawal *et al.* [1] consider the problem of multiple refraction planes, and model underwater cameras with axial camera models. Haner *et al.* [18] study the extrinsic calibration in presence of a single refraction. Chen and Yang [12] calibrate a stereo system in presence of a thick flat refraction plane. All these methods are developed for conventional cameras. In contrast, we develop underwater calibration and 3D reconstruction algorithms for light field cameras.

3. Method

We consider the setting that an in-air light field camera (either above the water surface or inside a watertight housing) capturing a scene submerged in water through a flat water-air interface. We first present our underwater light

field camera calibration algorithm that considers the refraction of light happens at the water-air interface. We then develop a depth estimation algorithm for recovering the 3D of underwater scenes.

3.1. Underwater Light Field Camera Calibration

Our calibration algorithm accounts for the refraction that occurs at the planar water-air interface (see Fig. 2). Our goal is to estimate the intrinsic parameters, extrinsic parameters, as well as a set of interface parameters that characterize the water-air interface and the refractive media.

The intrinsic parameters map a pixel on the image plane to a ray that exits the light field camera. We represent a ray with a point on the ray and its direction. We set the main lens plane as the $z = 0$ plane. A ray exiting the camera can be represented by its intersection with the main lens plane $P_a = (u, v, 0)^\top$, and its direction $\mathbf{d}_a = (\sigma, \tau, 1)^\top$. We decode the raw light field image into sub-aperture images. A sub-aperture image pixel can be represented as a 4D coordinate $(s, t, i, j)^\top$, where (s, t) is the sub-aperture image index, and (i, j) is the pixel index within a sub-aperture image. Dansereau *et al.* [15] derive that the mapping between an image pixel and its exiting ray under the homogeneous coordinate can be expressed as a 5×5 matrix H with 12 non-zero elements:

$$\begin{bmatrix} u \\ v \\ \sigma \\ \tau \\ 1 \end{bmatrix} = \begin{bmatrix} H_1 & 0 & H_2 & 0 & H_3 \\ 0 & H_4 & 0 & H_5 & H_6 \\ H_7 & 0 & H_8 & 0 & H_9 \\ 0 & H_{10} & 0 & H_{11} & H_{12} \\ 0 & 0 & 0 & 0 & 1 \end{bmatrix} \begin{bmatrix} s \\ t \\ i \\ j \\ 1 \end{bmatrix} \quad (1)$$

We further use the following distortion model to compensate for lens aberrations:

$$\begin{bmatrix} \sigma' \\ \tau' \end{bmatrix} = (1 + k_1 r^2 + k_2 r^4 + k_3 r^8) \begin{bmatrix} \sigma - b_1 \\ \tau - b_2 \end{bmatrix} + \begin{bmatrix} b_1 \\ b_2 \end{bmatrix} \quad (2)$$

where $(\sigma', \tau', 1)^\top$ is the compensated ray direction; $\{k_1, k_2, k_3, b_1, b_2\}$ are the distortion parameters; and $r^2 = (\sigma - b_1)^2 + (\tau - b_2)^2$. To simplify our notations, we drop the prime symbol and directly use $(\sigma, \tau, 1)^\top$ as the compensated ray direction in the latter paragraphs.

We refer the non-zero elements in H $\{H_1, \dots, H_{12}\}$ and the distortion parameters $\{k_1, k_2, k_3, b_1, b_2\}$ as the **intrinsic parameters** of a light field camera.

The in-air camera ray $\mathbf{r}_a : P_a + \lambda \mathbf{d}_a$ (where λ is the ray propagation factor) is refracted at the water-air interface. We then derive the origin and direction of the refracted ray. We represent the water-air interface with the plane equation: $Ax + By + Cz + D = 0$. By plugging \mathbf{r}_a into the plane equation, we can calculate the point P_w where the camera ray enters the water. The propagation factor λ_w for P_w is derived as:

$$\lambda_w = -\frac{Au + Bv + D}{A\sigma + B\tau + C} \quad (3)$$

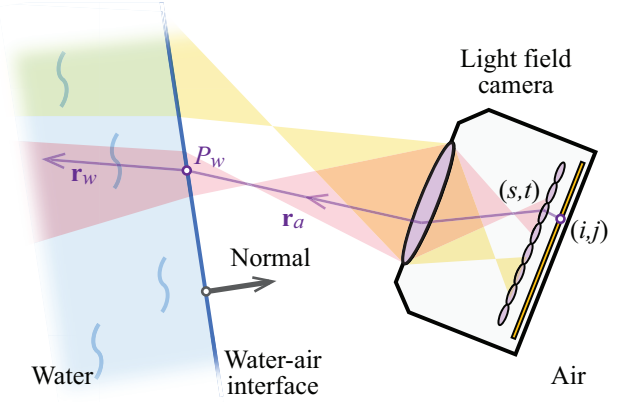


Figure 2. Underwater imaging setting. The in-air light field camera captures an underwater scene through a planar water-air interface. A camera ray \mathbf{r}_a becomes an underwater ray \mathbf{r}_w after refraction.

Therefore we have $P_w = P_a + \lambda_w \mathbf{d}_a$. We then use P_w as the origin of the refracted ray.

We apply the Snell's law to calculate the direction of the refracted ray. Given the camera ray direction \mathbf{d}_a , the plane normal $\mathbf{n} = (A, B, C)^\top / \sqrt{A^2 + B^2 + C^2}$, and the refractive index of water n (we assume the refractive index of air is 1), the refracted ray direction can be calculated as:

$$\mathbf{d}_w = \frac{1}{n} (\mathbf{d}_a - (\alpha + \sqrt{n^2 - (1 - \alpha^2)}) \mathbf{n}) \quad (4)$$

where $\alpha = \mathbf{n} \cdot \mathbf{d}_a$. The refracted ray (or underwater ray) is thus written as $\mathbf{r}_w : P_w + \lambda \mathbf{d}_w$.

Here we define the plane parameters $\{A, B, C, D\}$ and the refractive index of water n as the **interface parameters** as they determine how a ray is refracted at the water-air interface.

We then place a checkerboard inside the water for calibration. We use the **extrinsic parameters** $\{R|T\}$ (where $R \in \mathbb{R}^{3 \times 3}$ is a rotation matrix and $T \in \mathbb{R}^{3 \times 1}$ is a translation vector) to transform a point P_m on the checkerboard to the camera coordinate: $P = RP_m + T$. As P should lie on the underwater ray \mathbf{r}_w , we minimize the point-to-ray distance between P and \mathbf{r}_w to solve the calibration parameters (including intrinsic, interface, and extrinsic).

Specifically, we consider the point-to-ray distance in two cases (see Fig. 3). We first determine P is at which side of the interface plane. We compare the vector $\mathbf{l} = P - P_w$ with the plane normal \mathbf{n} . If \mathbf{l} and \mathbf{n} have opposite directions, P is on the water side; if they have the same direction, P is on the air side. Then, if P is on the water side (as it should be), we directly use its perpendicular distance from P to \mathbf{r}_w . If P is on air side (which must be caused by incorrect parameter estimation), we use the length of \mathbf{l} as its distance to \mathbf{r}_w . In this way, we penalize the estimations that cause P to be on the wrong side of the interface plane. The point-to-

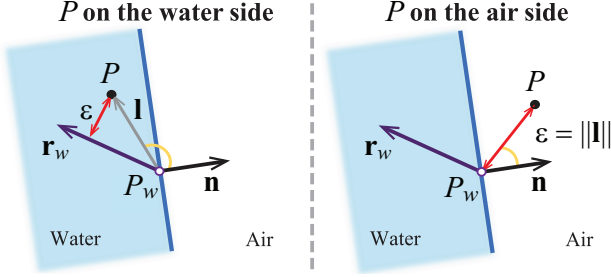


Figure 3. The point-to-ray distance $\varepsilon(P, \mathbf{r}_w)$ in the two cases.

ray distance $\varepsilon(P, \mathbf{r}_w)$ is therefore computed as:

$$\varepsilon(P, \mathbf{r}_w) = \begin{cases} \|\mathbf{l} - (\mathbf{l} \cdot \mathbf{d}_w)\mathbf{d}_w\|, & \mathbf{l} \cdot \mathbf{n} \leq 0 \\ \|\mathbf{l}\|, & \mathbf{l} \cdot \mathbf{n} > 0 \end{cases} \quad (5)$$

Suppose there are M feature points on the checkerboard, and we use N various poses. We sum up the point-to-ray errors as the objective function to be minimized:

$$\operatorname{argmin}_{\mathcal{I}, \mathcal{F}, \mathcal{E}} \sum_{\mathcal{I}} \sum_{\mathcal{F}, \mathcal{E}} \varepsilon(RP_m + T, \mathbf{r}_w) \quad (6)$$

Here $\mathcal{I} = \{H_{1,\dots,12} | k_{1,2,3}, b_{1,2}\}$ is intrinsic parameter set; $\mathcal{F} = \{A, B, C, D | n\}$ is the interface parameter set; and $\mathcal{E} = \{R_{1,\dots,N} | T_{1,\dots,N}\}$ is the extrinsic parameter set.

3.2. Underwater 3D Reconstruction

Once the light field camera is calibrated, we recover the 3D of underwater scene by estimating per-pixel depth values. Our 3D reconstruction algorithm takes the sub-aperture images $\{I_{s,t}\}_{s,t=1}^{S,T}$ as input. We estimate the per-pixel depth d in the center-view image $I_c = I_{s_c, t_c} (s_c = \lfloor \frac{S}{2} \rfloor, t_c = \lfloor \frac{T}{2} \rfloor)$. Our depth estimation algorithm utilizes two constraints: 1) color and gradient consistency along the epipolar lines, and 2) color uniformity of the angular patch retrieved from a common scene point.

Color consistency on curved epipolar lines. Unlike the in-air environment, the epipolar lines in our sub-aperture images are curved due to refraction [11]. We first fit the epipolar curves in sub-aperture images. Given a pixel $p = (i, j)$ in I_c , we trace an underwater ray \mathbf{r}_w using our derivations in Section 3.1. We then sample a set of points on \mathbf{r}_w (we sample 5 points in our implementation), and trace rays back to other sub-aperture images. In each sub-aperture image (except for I_c), we use these projections as control points to fit the epipolar curve $f_{s,t}^p$. As the curvatures of the epipolar curves are usually small, we pick the sample points with large depth intervals. This process is illustrated in Fig. 4. Assuming the corresponding points have consistent color and gradient of color, we use the color and gradient differences between p and candidate points along its

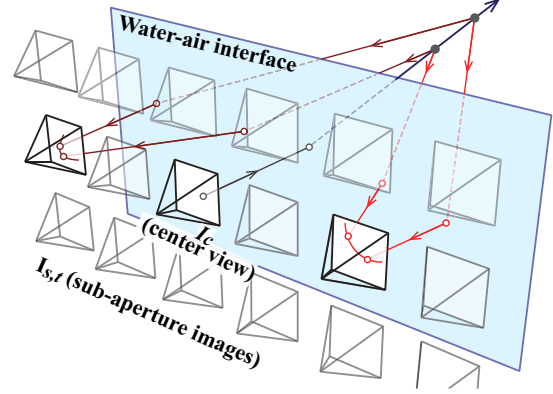


Figure 4. Epipolar lines are curved due to refraction. We map an underwater ray from the center view I_c to other sub-aperture images to find the epipolar curves.

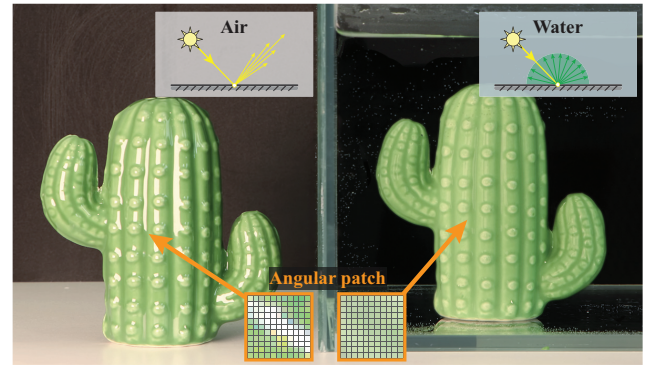


Figure 5. Underwater scenes exhibit very weak specular reflection. We show photographs of the same object captured in air (left) vs. underwater (right). We also show the angular patch of a sample point in the two cases.

epipolar curves $f_{s,t}^p$ as error measurements:

$$E_{color}(p, d) = \sum_{t=1}^T \sum_{s=1}^S |I_c(p) - I_{s,t}(f_{s,t}^p(d))| \quad (7)$$

$$E_{grad}(p, d) = \sum_{t=1}^T \sum_{s=1}^S |G_c(p) - G_{s,t}(f_{s,t}^p(d))| \quad (8)$$

where G is the combined gradient of a sub-aperture image I (i.e., $G = \partial I / \partial x + \partial I / \partial y$).

Angular uniformity constraint. We observe that the view-dependent specular reflection of underwater scenes is much weaker than the in-air scenes (see Fig. 5). One possible reason is that the refractive index gradient between water and most natural objects is much lower than the gradient in air [40, 14]. We therefore introduce the angular uniformity constraint, in light of an underwater scene point having uniform reflectance towards all directions.

An angular patch is an array of pixels taken from all sub-aperture images, assuming that they correspond to the same 3D scene point. We can find the angular patch $A(d)$ of a scene point P_d at depth d by tracing rays from P_d to the sub-aperture images (see Fig. 6 (b)). However, such mapping is computationally expensive, as the projection function from d to an image pixel (i, j) in sub-aperture (s, t) : $(i, j) = \mathcal{H}(d; s, t)$ is highly nonlinear (see the derivation of \mathcal{H} in the supplementary material). Our implementation takes around $9sec$ to retrieve one patch. The running time for generating all patches for possible depth candidates, and for all scene points is thus prohibitively long. Whereas the simple linear ray propagation, although fast ($0.06sec$ per patch), results in wrong angular samples (see Fig. 6 (a)). We therefore develop a fast algorithm based on the first-order approximation for angular patch retrieval.

We illustrate our approximation algorithm in Fig. 6 (c). The idea is to find the intersection point P_w at the water-air interface, for each sub-aperture image using the Euler’s method, then linearly map P_w to (i, j) as the light path segment in air is linear. We start from the central view I_c . We first determine the intersection point P_w^c for the central view using Eq. 3. We then formulate an equation that maps d to $P_w = (x, y, z)$ with respect to each sub-aperture image (s, t) : $(x, y, z) = \mathcal{G}(d; s, t)$ (see the derivation of \mathcal{G} in the supplementary material). We then propagate P_w for neighboring views as: $(x, y, z)_{s+1, t+1} = (x, y, z)_{s, t} + \Delta s \frac{\partial \mathcal{G}}{\partial s} + \Delta t \frac{\partial \mathcal{G}}{\partial t}$. Here $(x, y, z)_{s+1, t+1}$ is the intersection point for the view $(s+1, t+1)$, which is the point we plan to propagate; $(x, y, z)_{s, t}$ is the intersection point for the view (s, t) , which we’ve already known (e.g., P_w^c in the first iteration); Δs and Δt are the horizontal and vertical baselines between the sub-aperture views; $\frac{\partial \mathcal{G}}{\partial s}$ and $\frac{\partial \mathcal{G}}{\partial t}$ are the first-order partial derivatives of \mathcal{G} with respect to s and t . In this way, we are able to find P_w with linear equations. Our fast algorithm edges the accuracy of non-linear mapping, but with similar speed as the linear method ($0.07sec$ per patch). The Euler’s method can produce highly accurate approximation because the baselines of compact light field cameras are uniform and small.

After retrieving the angular patch, we compute the variance of the patch. As the angular patch usually has uniform color, its variance should be small if it is retrieved from the correct depth. In Fig. 6 (e) we show the patch variance with respect to the depth values. We can see that both the non-linear mapping and our first-order approximation have the lowest variance (close to zero) at the true depth. The linearly mapped patch has constant high variance as the angular sample are not correctly retrieved. We thus define the angular uniformity constraint as the sum of angular patch variances. This objective function is written as:

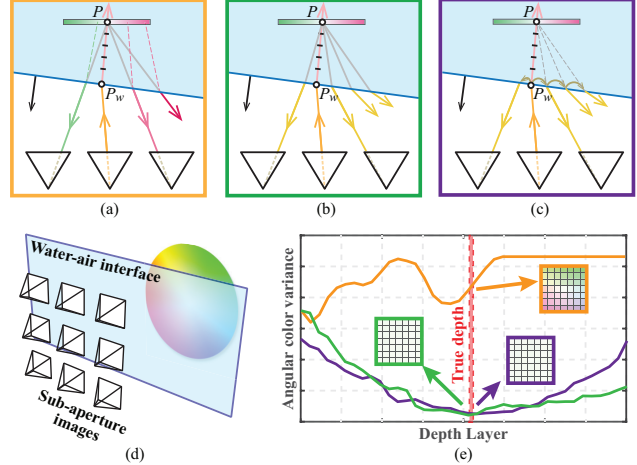


Figure 6. Angular patch retrieval. We show three schemes (a), (b), and (c) for retrieving angular patches given the setting shown in (d). (a) shows the linear ray tracing that results in wrong angular samples. (b) shows the non-linear ray tracing that considers the refraction (but is slow). (c) shows our approximation that linearly propagates to neighboring views, which is both fast and accurate. (e) shows the color variance w.r.t. the depth for the angular patches retrieved using (a), (b), and (c).

$$E_{angular}(p, d) = \frac{1}{ST-1} \sum_{t=1}^T \sum_{s=1}^S |A_{s,t}^p(d) - \mu|^2 \quad (9)$$

where $A^p(d)$ is the angular patch for a pixel p in I_c , retrieved at depth d ; μ is the mean of $A^p(d)$.

Optimization. We combine Eq. 7, 8, 9, and an additional smooth term as the overall objective function for depth estimation:

$$\arg \min_d \sum_p (\beta_1 E_{color} + \beta_2 E_{grad} + \beta_3 E_{angular} + \beta_4 E_{smooth}) \quad (10)$$

where $\beta_{1, \dots, 4}$ are weights for balancing the four terms; $E_{smooth} = \sum_{p_{\mathcal{N}}} ||d(p) - d(p_{\mathcal{N}})||$ ($p_{\mathcal{N}}$ is the set of neighboring pixels around p) is the smooth term that enforces the depth smoothness.

To solve this optimization problem, we first use a guided filter [19] with I_c as reference to smooth the error measurements (E_{color} , E_{grad} , and $E_{angular}$). We then use the multi-label graph cut algorithm [25] to optimize Eq. 10 for depth estimation.

4. Experiments

We perform both synthetic and real experiments to evaluate our approach. We also compare against the state-of-the-arts calibration and 3D reconstruction methods.

Table 1. Estimated intrinsic parameters under interface setting \mathcal{F}_3 .

	SV	TB	MPC	Ours	GT
b	-	4.2716e-4	4.1310e-4	4.0003e-4	4.00e-4
f_x	789.2850	776.4190	787.9620	550.5019	550
f_y	789.8730	766.5866	788.5638	550.5043	550
c_x	354.9465	312.5197	354.2245	313	312.5
c_y	249.9410	217.5023	249.5642	217.5	217

4.1. Synthetic Experiments

We simulate light field images of underwater scenes through ray tracing. Our light field images have 11×11 sub-aperture images with resolution 625×434 . The equivalent baseline is $b = 0.4mm$. We set the center of projection the center view image as the original of the camera coordinate.

We set the refractive index of air to 1. We use three sets of interface parameters with different plane orientations and refractive indices of water: $\mathcal{F}_1 = \{0, 0, -1, 0.1|1.333\}$, $\mathcal{F}_2 = \{0, 0, -1, 0.1|1.45\}$, and $\mathcal{F}_3 = \{0.1476, 0.0984, -0.9841, 0.1|1.333\}$. \mathcal{F}_1 and \mathcal{F}_2 use frontal-parallel interface planes, but different refractive indices of water. \mathcal{F}_3 uses an oblique interface plane.

Underwater Calibration. We place a 6×7 checkerboard at the waterside. We randomly pick rotation and translation matrices to generate different pattern poses.

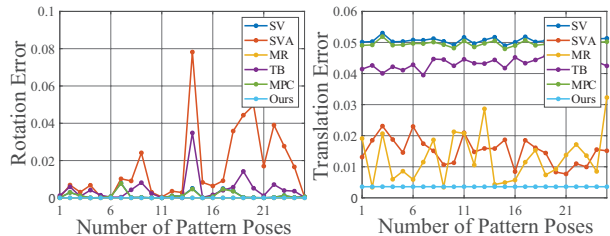
We compare our intrinsic calibration with three state-of-the-art methods: 1) **SV** [7]: a classical calibration method for conventional camera at a single viewpoint; 2) **TB** [15]: the calibration algorithm from the Light Field Toolbox for Matlab; and 3) **MPC** [55]: a recent light field camera calibration method that uses a multi-projection-center model to reduce the parameter space. All these methods are designed for in-air calibration without considering the refraction of light. We use the center view image as input to the single view method (SV).

Table 1 shows the intrinsic calibration results in comparison with the ground truth under the interface setting \mathcal{F}_3 . See the supplementary material for results under \mathcal{F}_1 and \mathcal{F}_2 , as well as the conversion from our intrinsic matrix to the standard parameterization. We can see that the estimated baselines are less affected by the refraction. The estimated focal lengths from all air-based methods are closer to the ground truth values multiplied by the refractive index (1.333). In contrast, our method separates the refraction and is able to estimate more accurate intrinsic parameters.

As our method also calibrates the interface parameters \mathcal{F} (including the interface plane parameters and the refractive index of water), we show our calibration results under the three interface setting in comparison with the ground truths in Table 2. We can see that our estimations are accurate. Our method is robust under various interface orientations and refractive indices.

Table 2. Estimated interface parameters under all three settings.

	\mathcal{F}_1		\mathcal{F}_2		\mathcal{F}_3	
	GT	Ours	GT	Ours	GT	Ours
A	0	-0.0014	0	-0.0014	0.1476	0.1470
B	0	-0.0018	0	-0.0011	0.0984	0.0975
C	-1	-1	-1	-1	-0.9841	-0.9843
D	0.1	0.1001	0.1	0.1001	0.1	0.1005
n	1.333	1.3364	1.45	1.4601	1.333	1.3384

Figure 7. Errors of extrinsic parameter estimation under interface setting \mathcal{F}_3 .

Finally, we evaluate our extrinsic parameter calibration. Here we also compare with two other methods that assume known intrinsics: 1) **SVA**: the classical calibration method [7] that uses the ground truth intrinsic parameters in air; and 2) **MR** [1]: the multi-refractive layer underwater calibration method that uses the ground truth intrinsic and interface parameters. For each method, we evaluate the estimated rotation and translation with respect to different numbers of pattern poses. The extrinsic parameter estimation errors under the interface setting \mathcal{F}_3 are in Fig. 7. Please refer to the supplementary material for errors under the other two interface settings, and the visualization of extrinsic calibration results.

Depth Estimation. Given the calibration parameters, we evaluate our depth estimation algorithm. In this experiment, we use the interface parameter $\mathcal{F}_1 = \{0, 0, -1, 0.1|1.333\}$, and test on a planar target. We compare with a state-of-the-art light field based depth estimation method [22]. For fair comparison, we first use their algorithm to estimate a disparity map. We then use the ground truth intrinsic parameters and refract the light at the water-air interface to convert the disparities to depth values. The reconstruction results in comparison with the ground truth plane are shown in Fig. 8. We can see that our reconstruction result is highly close to the ground truth plane. The result of [22] is close to the ground truth plane at the center as the central rays are less refracted when the interface plane is frontal parallel. However, their reconstruction appears curved because the method assumes straight epipolar lines that doesn't account for the refraction.

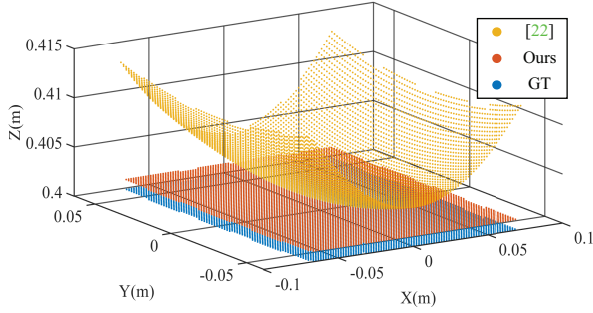


Figure 8. 3D reconstruction of an underwater plane.

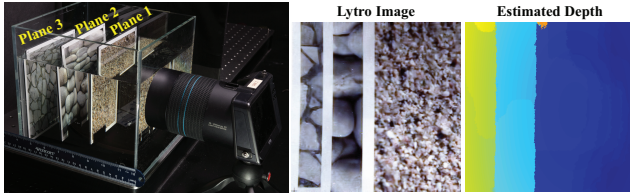


Figure 9. Quantitative evaluation on three depth layers. From left to right: scene setting, center view of the captured light field, and our estimated depth map.

4.2. Real Experiments

We perform real experiments to validate our algorithms. We use the Lytro Illum to capture underwater scenes submerged in a water tank of size $60\text{cm} \times 30\text{cm} \times 36\text{cm}$. Our experimental setup is shown in Fig. 1. The captured light field image has resolution 7728×5368 . We decode it to 15×15 sub-aperture images, each with resolution 625×434 . Please see the supplementary material for our camera calibration results.

Quantitative Evaluation. We quantitatively evaluate our method using underwater planar board at three different depths (see Fig. 9). The ground truth depths are measured with a ruler. Our estimated depth map is shown in Fig. 9. We measure the depth estimation error in mm by comparing our estimated depths with the ground truth. We also perform ablation studies on the terms in our objective function (Eq. 10). The depth estimations errors for the three planar boards are reported in Table 3. We can see that our proposed angular uniformity constraint ($E_{angular}$) effectively improves the reconstruction accuracy. Our error increases as the true depth increases.

We then evaluate our depth estimation error with denser depth layers. Specifically, we use a translational rail that horizontally move a planar board with 2cm step. The setting is shown in Fig. 10. The tested depth range is from 8cm to 18cm . We perform depth reconstruction at each depth layers. We evaluate our estimated depth by comparing with the ground truth value. Our recovered point cloud is shown in Fig. 10. We visualize the point cloud with the point’s depth

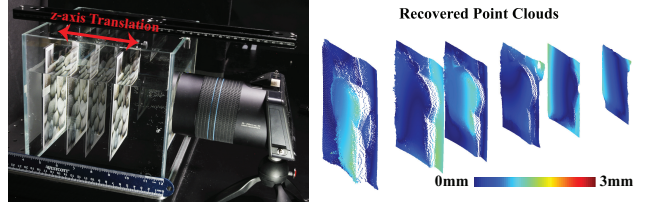


Figure 10. Quantitative evaluation on dense depth layers. Left: scene setting; Right: our recovered point visualized in depth estimation error.

Table 3. Ablation study on the terms in our objective function. We report the depth estimation errors in mm .

Regularization terms	Plane 1 at 9cm	Plane 2 at 15cm	Plane 3 at 20cm
w/o $E_{angular}, E_{smooth}$	2.8587	7.7169	10.9305
w/o $E_{angular}$	1.9112	6.5741	7.8348
w/o E_{smooth}	1.8294	2.3673	3.2337
Ours (all terms included)	1.7852	1.1930	2.4445

error. The max error of all points is 5.5mm , and the mean error is 0.9mm . This demonstrates that our depth estimation algorithm has good accuracy.

Underwater Scene Reconstruction. We first use one light field camera to capture the 3D of various underwater scenes. We compare our results with two active 3D reconstruction methods: the time-of-flight (ToF) and the structured light. For ToF, we use the Azure Kinect to scan our underwater scene. We recover the point cloud using the default SDK. For structured light, we build a projector-camera system for 3D scanning. In the system, we use a 1920×1080 laser projector and a 1600×1200 color camera. Both the projector and the camera are calibrated with underwater patterns [31]. We project the Gray code patterns to the scene, and recover the point cloud through ray triangulation without considering the refraction.

The recovered point clouds are shown in Fig. 11. The structured light scanning results are not shown with color as the projected pattern distorts the original color of the scene. We can see that the ToF results suffer from large errors because the velocity of light in water is smaller than that in air. Without compensating this factor, the estimated depths are erroneous. For the structured light reconstruction, we find that the Gray code decoding is quite accurate. However, the recovered point clouds are sparse because without compensating the refraction, many rays cannot intersect in space. In contrast, our approach produces 3D models that resemble the scene objects.

We also perform experiments with two light field cameras. The two cameras are placed side by side in order to have large overlap in the field of view. We perform 3D reconstruction on each light field, show that the reconstructed

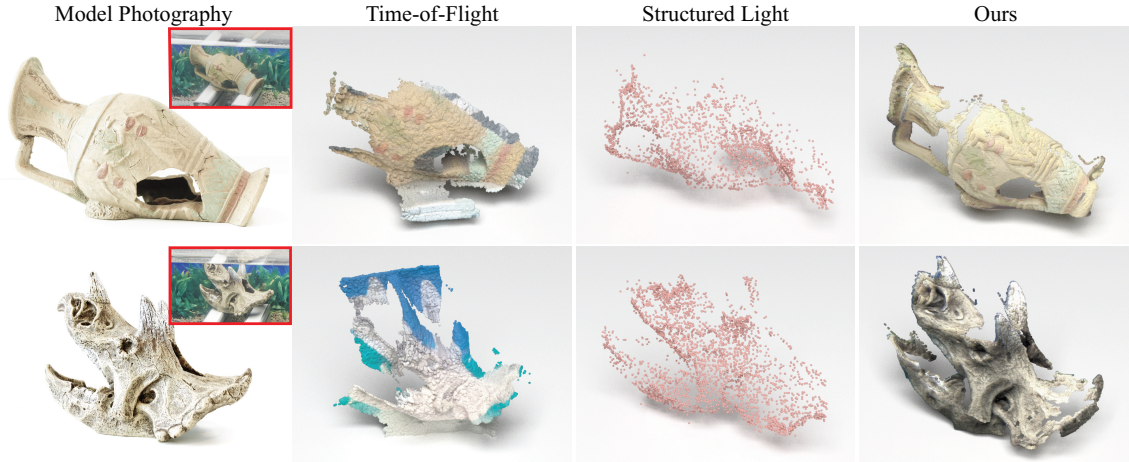


Figure 11. 3D Reconstruction results with one light field camera in comparison with the time-of-flight and the structured light results. We also show photographs of the objects and the underwater scenes.

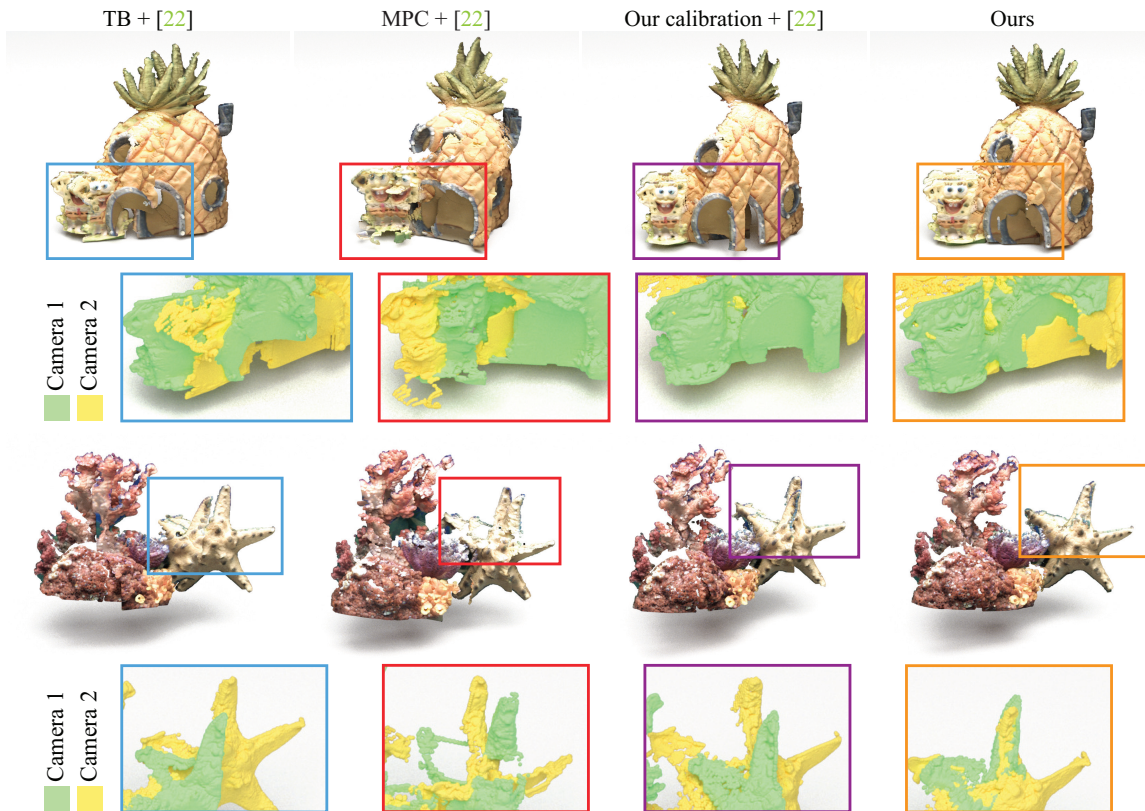


Figure 12. Point cloud fusion results with two light field cameras. We directly combine the point clouds without applying fitting algorithms. We show zoom-in views that display the two point clouds in different colors.

point clouds can be naturally aligned without using any fitting algorithms (*e.g.*, the iterative closest point (ICP) [4]). For comparison, we combine two light field camera calibration algorithms (TB [15] and MPC [22]) with a light field based depth estimation algorithm [22]. We perform TB with in-air calibration targets, while MPC with underwater ones. We also combine [22] with our calibration re-

sults. Note that as the interface parameters are not available in TB and MPC, we are unable to consider refraction when applying [22]. The point cloud fusion results are shown in Fig. 12. We can see that the fusion results from all comparison methods exhibit obvious mis-alignments. In contrast, our reconstructed point clouds can be well aligned without explicit fitting.

References

- [1] Amit Agrawal, Srikumar Ramalingam, Yuichi Taguchi, and Visesh Chari. A theory of multi-layer flat refractive geometry. In *IEEE Conference on Computer Vision and Pattern Recognition (CVPR)*, 2012.
- [2] Yuta Asano, Yinqiang Zheng, Ko Nishino, and Imari Sato. Shape from water: Bispectral light absorption for depth recovery. In *European Conference on Computer Vision (ECCV)*, 2016.
- [3] Yuta Asano, Yinqiang Zheng, Ko Nishino, and Imari Sato. Depth sensing by near-infrared light absorption in water. *IEEE Transactions on Pattern Analysis and Machine Intelligence*, 2020.
- [4] Paul J. Besl and Neil D. McKay. A method for registration of 3-D shapes. *IEEE Transactions on Pattern Analysis and Machine Intelligence*, 14(2):239–256, 1992.
- [5] Yunsu Bok, Hae-Gon Jeon, and In So Kweon. Geometric calibration of micro-lens-based light-field cameras using line features. In *European Conference on Computer Vision (ECCV)*, 2014.
- [6] Yunsu Bok, Hae-Gon Jeon, and In So Kweon. Geometric calibration of micro-lens-based light field cameras using line features. *IEEE Transactions on Pattern Analysis and Machine Intelligence*, 39(2):287–300, 2016.
- [7] Jean-Yves Bouguet. Camera calibration toolbox for matlab, http://www.vision.caltech.edu/bouguetj/calib_doc/index.html.
- [8] Chris Buehler, Michael Bosse, Leonard McMillan, Steven Gortler, and Michael Cohen. Unstructured lumigraph rendering. In *28th Annual Conference on Computer Graphics and Interactive Techniques*, 2001.
- [9] François Chadebecq, Francisco Vasconcelos, George Dwyer, René Lacher, Sébastien Ourselin, Tom Vercauteren, and Danail Stoyanov. Refractive structure-from-motion through a flat refractive interface. In *IEEE International Conference Computer Vision (ICCV)*, 2017.
- [10] François Chadebecq, Francisco Vasconcelos, René Lacher, Efthymios Maneas, Adrien Desjardins, Sébastien Ourselin, Tom Vercauteren, and Danail Stoyanov. Refractive two-view reconstruction for underwater 3D vision. *International Journal of Computer Vision*, pages 1101–1117, 2019.
- [11] Visesh Chari and Peter Sturm. Multiple-view geometry of the refractive plane. In *British Machine Vision Conference (BMVC)*, 2009.
- [12] Xida Chen and Yee-Hong Yang. Two-view camera housing parameters calibration for multi-layer flat refractive interface. In *IEEE Conference on Computer Vision and Pattern Recognition (CVPR)*, 2014.
- [13] Silvia Cocito, Sergio Sgorbini, Andrea Peirano, and Mario Valle. 3-D reconstruction of biological objects using underwater video technique and image processing. *Journal of Experimental Marine Biology and Ecology*, 297(1):57–70, 2003.
- [14] Thomas W. Cronin, Nadav Shashar, Roy L. Caldwell, Justin Marshall, Alexander G. Cheroske, and Tsyr-Huei Chiou. Polarization vision and its role in biological signaling. *Integrative and Comparative Biology*, 43(4):549–558, 2003.
- [15] Donald G. Dansereau, Oscar Pizarro, and Stefan B. Williams. Decoding, calibration and rectification for lenselet-based plenoptic cameras. In *IEEE Conference on Computer Vision and Pattern Recognition (CVPR)*, 2013.
- [16] Renata Ferrari, David McKinnon, Hu He, Ryan N. Smith, Peter Corke, Manuel González-Rivero, Peter J Mumby, and Ben Upcroft. Quantifying multiscale habitat structural complexity: a cost-effective framework for underwater 3D modelling. *Remote Sensing*, 8(2):113, 2016.
- [17] Jason Gedge, Minglun Gong, and Yee-Hong Yang. Refractive epipolar geometry for underwater stereo matching. In *Canadian Conference on Computer and Robot Vision*, 2011.
- [18] Sebastian Haner and Kalle Åström. Absolute pose for cameras under flat refractive interfaces. In *IEEE Conference on Computer Vision and Pattern Recognition (CVPR)*, 2015.
- [19] Kaiming He, Jian Sun, and Xiaoou Tang. Guided image filtering. *IEEE Transactions on Pattern Analysis and Machine Intelligence*, 35(6):1397–1409, 2012.
- [20] Jon Henderson, Oscar Pizarro, Matthew Johnson-Roberson, and Ian Mahon. Mapping submerged archaeological sites using stereo-vision photogrammetry. *International Journal of Nautical Archaeology*, 42(2):243–256, 2013.
- [21] Kazuto Ichimaru, Yuichi Taguchi, and Hiroshi Kawasaki. Unified underwater structure-from-motion. In *IEEE International Conference on 3D Vision (3DV)*, 2019.
- [22] Hae-Gon Jeon, Jaesik Park, Gyeongmin Choe, Jinsun Park, Yunsu Bok, Yu-Wing Tai, and In So Kweon. Accurate depth map estimation from a lenslet light field camera. In *IEEE Conference on Computer Vision and Pattern Recognition (CVPR)*, 2015.
- [23] Matthew Johnson-Roberson, Oscar Pizarro, Stefan B Williams, and Ian Mahon. Generation and visualization of large-scale three-dimensional reconstructions from underwater robotic surveys. *Journal of Field Robotics*, 27(1):21–51, 2010.
- [24] Anne Jordt-Sedlazeck and Reinhard Koch. Refractive structure-from-motion on underwater images. In *IEEE International Conference Computer Vision (ICCV)*, 2013.
- [25] Vladimir Kolmogorov and Ramin Zabih. Multi-camera scene reconstruction via graph cuts. In *European Conference on Computer Vision (ECCV)*, 2002.
- [26] Jean-Marc Lavest, Gérard Rives, and Jean-Thierry Lapresté. Underwater camera calibration. In *European Conference on Computer Vision (ECCV)*.
- [27] Marc Levoy and Pat Hanrahan. Light field rendering. In *23rd Annual Conference on Computer Graphics and Interactive Techniques*, 1996.
- [28] Zhouchen Lin and Heung-Yeung Shum. A geometric analysis of light field rendering. *International Journal of Computer Vision*, pages 121–138, 2004.
- [29] Andrew Lumsdaine and Todor Georgiev. The focused plenoptic camera. In *IEEE International Conference on Computational Photography*, 2009.
- [30] John McCarthy. Multi-image photogrammetry as a practical tool for cultural heritage survey and community engagement. *Journal of Archaeological Science*, 43:175–185, 2014.

- [31] Daniel Moreno and Gabriel Taubin. Simple, accurate, and robust projector-camera calibration. In *Second International Conference on 3D Imaging, Modeling, Processing, Visualization Transmission*, 2012.
- [32] Srinivasa G. Narasimhan and Shree K. Nayar. Structured light methods for underwater imaging: light stripe scanning and photometric stereo. In *Proceedings of the MTS/IEEE Oceans*, pages 2610–2617, 2005.
- [33] Shahriar Negahdaripour and Hossein Madjidi. Stereovision imaging on submersible platforms for 3-D mapping of benthic habitats and sea-floor structures. *IEEE Journal of Oceanic Engineering*, 28(4):625–650, 2003.
- [34] Ren Ng. Fourier slice photography. In *ACM SIGGRAPH*, pages 735–744, 2005.
- [35] Ren Ng, Marc Levoy, Mathieu Brédif, Gene Duval, Mark Horowitz, Pat Hanrahan, et al. Light field photography with a hand-held plenoptic camera. *Computer Science Technical Report CSTR*, 2(11):1–11, 2005.
- [36] Liam Paull, Sajad Saeedi, Mae Seto, and Howard Li. Auv navigation and localization: A review. *IEEE Journal of Oceanic Engineering*, 39(1):131–149, 2013.
- [37] Oscar Pizarro, Ryan Michael Eustice, and Hanumant Singh. Large area 3-D reconstructions from underwater optical surveys. *IEEE Journal of Oceanic Engineering*, 34(2):150–169, 2009.
- [38] Yiming Qian, Yinqiang Zheng, Minglun Gong, and Yee-Hong Yang. Simultaneous 3D reconstruction for water surface and underwater scene. In *European Conference on Computer Vision (ECCV)*, 2018.
- [39] Amin Sarafraz and Brian K Haus. A structured light method for underwater surface reconstruction. *ISPRS Journal of Photogrammetry and Remote Sensing*, 114:40–52, 2016.
- [40] Yoav Y. Schechner and Nir Karpel. Recovery of underwater visibility and structure by polarization analysis. *IEEE Journal of Oceanic Engineering*, pages 570–587, 2005.
- [41] Anne Sedlazeck and Reinhard Koch. Calibration of housing parameters for underwater stereo-camera rigs. In *British Machine Vision Conference (BMVC)*, 2011.
- [42] Katherine A. Skinner and Matthew Johnson-Roberson. Underwater image dehazing with a light field camera. In *IEEE Conference on Computer Vision and Pattern Recognition Workshop (CVPRW)*, 2017.
- [43] Yohay Swirski, Yoav Y. Schechner, Ben Herzberg, and Shahriar Negahdaripour. Caustereo: Range from light in nature. *Applied Optics*, 50(28):89–101, Oct 2011.
- [44] Michael W Tao, Sunil Hadap, Jitendra Malik, and Ravi Ramamoorthi. Depth from combining defocus and correspondence using light-field cameras. In *IEEE International Conference Computer Vision (ICCV)*, 2013.
- [45] Tali Treibitz, Yoav Y. Schechner, Clayton Kunz, and Hanumant Singh. Flat refractive geometry. *IEEE Transactions on Pattern Analysis and Machine Intelligence*, 34(1):51–65, 2011.
- [46] Tali Treibitz, Yoav Y. Schechner, and Hanumant Singh. Flat refractive geometry. In *IEEE Conference on Computer Vision and Pattern Recognition (CVPR)*, 2008.
- [47] Vigil Varghese, Mitch Bryson, Oscar Pizarro, Stefan B Williams, and Donald G Dansereau. Light field image restoration for vision in scattering media. In *IEEE International Conference of Image Processing*, 2018.
- [48] Ashok Veeraraghavan, Ramesh Raskar, Amit Agrawal, Ankit Mohan, and Jack Tumblin. Dappled photography: Mask enhanced cameras for heterodyned light fields and coded aperture refocusing. *ACM Transaction on Graphics*, 26(3):69, 2007.
- [49] Kartik Venkataraman, Dan Lelescu, Jacques Duparré, Andrew McMahan, Gabriel Molina, Priyam Chatterjee, Robert Mullis, and Shree Nayar. Picam: An ultra-thin high performance monolithic camera array. *ACM Transaction on Graphics*, 32(6):1–13, 2013.
- [50] Ting-Chun Wang, Alexei A Efros, and Ravi Ramamoorthi. Occlusion-aware depth estimation using light-field cameras. In *IEEE International Conference Computer Vision (ICCV)*, 2015.
- [51] Li-Yi Wei, Chia-Kai Liang, Graham Myhre, Colvin Pitts, and Kurt Akeley. Improving light field camera sample design with irregularity and aberration. *ACM Transaction on Graphics*, 34(4):1–11, 2015.
- [52] Bennett Wilburn, Neel Joshi, Vaibhav Vaish, Eino-Ville Talvala, Emilio Antunez, Adam Barth, Andrew Adams, Mark Horowitz, and Marc Levoy. High performance imaging using large camera arrays. In *ACM SIGGRAPH*, pages 765–776, 2005.
- [53] Kotaro Yamafune, Rodrigo Torres, and Filipe Castro. Multi-image photogrammetry to record and reconstruct underwater shipwreck sites. *Journal of Archaeological Method and Theory*, 24(3):703–725, 2017.
- [54] Mingjie Zhang, Xing Lin, Mohit Gupta, Jinli Suo, and Qionghai Dai. Recovering scene geometry under wavy fluid via distortion and defocus analysis. In *European Conference on Computer Vision (ECCV)*, 2014.
- [55] Qi Zhang, Chunping Zhang, Jinbo Ling, Qing Wang, and Jingyi Yu. A generic multi-projection-center model and calibration method for light field cameras. *IEEE Transactions on Pattern Analysis and Machine Intelligence*, 41(11):2539–2552, 2018.